Far-field coseismic forcing of giant rockslides in the 2017 Sarpol-Zahab Earthquake (Iran)

Aya Cheaib[1,3], Pascal Lacroix[1], Swann Zerathe[1], Denis Jongmans[1], Najmeh Ajorlou[2], Marie-Pierre Doin[1], James Hollingsworth[1], and Chadi Abdallah[3]

[1]ISTerre - Université Grenoble Alpes, IRD, CNRS, IFSTTAR, Université Savoie Mont Blanc, CS 40700, 38058 GRENOBLE Cedex 9 Grenoble, France.

[2]Department of earth science, Institute for Advanced Studies in Basic Sciences(IASBS), 444 Prof. Yousef Sobouti Blvd., Zanjan 45137-66731, Iran.

[3]Lebanese National Council for Scientific Research/Remote Sensing Center, Blvrd Sport City, Bir Hassan, P.O. Box 11-8281, Beirut, Lebanon.

Corresponding author: Aya Cheaib (aya.cheaib@univ-grenoble-alpes.fr)

Key Points:

- Novel approach for generating a comprehensive earthquake-induced landslide inventory (by combining various satellite data and methods).
- The forcing of several giant pre-existing rockslides in the far-field (140 to 180 km) of the Sarpol-Zahab earthquake epicenter.

Abstract

On November 12th 2017, the largest earthquake (Mw 7.3) ever recorded in the Zagros mountains occurred near the town of Sarpol-Zahab, Iran. While this region encompasses clusters of giant ancient rockslides, this seismic event is an excellent case-study to decipher the controlling factors of earthquake-induced landslides. Here, we address this issue by deriving an original earthquake-induced landslide inventory, encompassing landslides of various velocities (from rapid rockfalls to slow-moving landslides). This inventory displays clear differences in the spatial and volumetric distributions of earthquake-induced landslides, with 360 rockfalls triggered around the epicenter, and 9 giant active and ancient rockslides coseismically accelerated at locations up to 180 km from the epicenter. This distant triggering is explained by the earthquake source properties coupled with the local geological conditions. Our study documents a rare example of slow-moving landslides accelerated by an earthquake, and opens perspectives for the study of the landslide triggering over various time-scales.

Plain Language Summary

Landslides are one of the main secondary effects of earthquakes, with up to several thousands of landslides triggered during large magnitude earthquakes. The spatial and size distribution of these landslides is function of the earthquake source and site specificities. The factors that control earthquake-induced landslides can be diverse and combine in complex ways. In this study, we address this issue by focusing on the landslides induced by the Mw7.3 Sarpol-Zahab earthquake that struck the Zagros mountains (Iran/Irak border) on November 12th 2017. We developed an original approach to detect and monitor landslides of different velocities, from rapid rockfalls (m/s) to slow-moving landslides (m/yr to mm/yr), by using a set of various

satellite data and techniques. The striking elements of our landslide inventory is (1) the very little number of slope movements induced by the shaking, and (2) the unprecedented detection of giant rockslides (~ 10^9 m^3) in the far-field of an earthquake. This distant triggering is explained by a combination of the earthquake source properties coupled with the local geological conditions. These giant and slow-moving landslides, which have probably been active for several millennia, are unique objects for the study of earthquake forcing on landslides over time.

1 Introduction

Slope failures are one of the main secondary effects of earthquakes (Marano et al., 2010), with a large part of co- and post-seismic damage caused by landslides in mountainous areas (Fan et al., 2019; Keefer, 2002; Marc et al., 2015). Many factors can contribute to the heterogeneous spatial distribution of earthquake-induced landslides: geology (Roback et al., 2018), topography (Meunier et al., 2008), groundwater (e.g., Wang et al., 2014), and earthquake source characteristics (e.g., Gorum et al., 2011). In addition, shaking can have delayed effects on slope stability at time scales from days to years. These effects may include changes in groundwater circulation (Wang & Chia, 2008), a modification in soil permeability (Rojstaczer & Wolf, 1992), or a degradation of the mechanical properties of the slope thereby making it more susceptible to landslides in future earthquakes (Bontemps et al., 2020; Marc et al., 2015). The quantification of these controlling factors and their subsequent mechanisms is, however, based on a limited number of earthquake-induced landslide inventories (e.g. Tanyas et al., 2017), and on the instrumentation of a small number of low-velocity active landslides in seismic areas (Bontemps et al., 2020; Lacroix et al., 2014), thus highlighting the need to document and analyze more earthquake-induced landslides across a wider range of seismic and climatic settings.

On November 12th 2017, a Mw7.3 earthquake struck the northwestern part of the Zagros Mountains, close to the town of Sarpol-Zahab (Figure 1). This major earthquake occurred at the end of the dry season in a semi-arid area that encompasses a high density of giant paleo-landslides of volumes between 0.01-30 km^3 affecting mostly carbonate lithology (Ghazipour & Simpson, 2016). Following this earthquake, a few coseismic landslides of various types (debris fall, boulder/rock fall) were reported near the epicenter (Miyajima et al., 2018; Vajedian et al., 2018). The earthquake triggered the giant Mela-Kabod landslide (4-km-long, 1-km-wide) ~40 km south of the epicenter, with a coseismic displacement of ~30 m (Goorabi, 2020; Vajedian et al.,2018). No reactivation was reported for the many other giant landslides in this region.

The large Sarpol-Zahab earthquake provides a unique opportunity to study the forcing mechanisms of landslides under strong seismic stressing in a semi-arid region. To this end, we have used optical satellite and multi-temporal InSAR methods to establish a complete inventory of rapid (~m/s) and slow (~mm to m/yr) landslides and investigate their response to the earthquake.

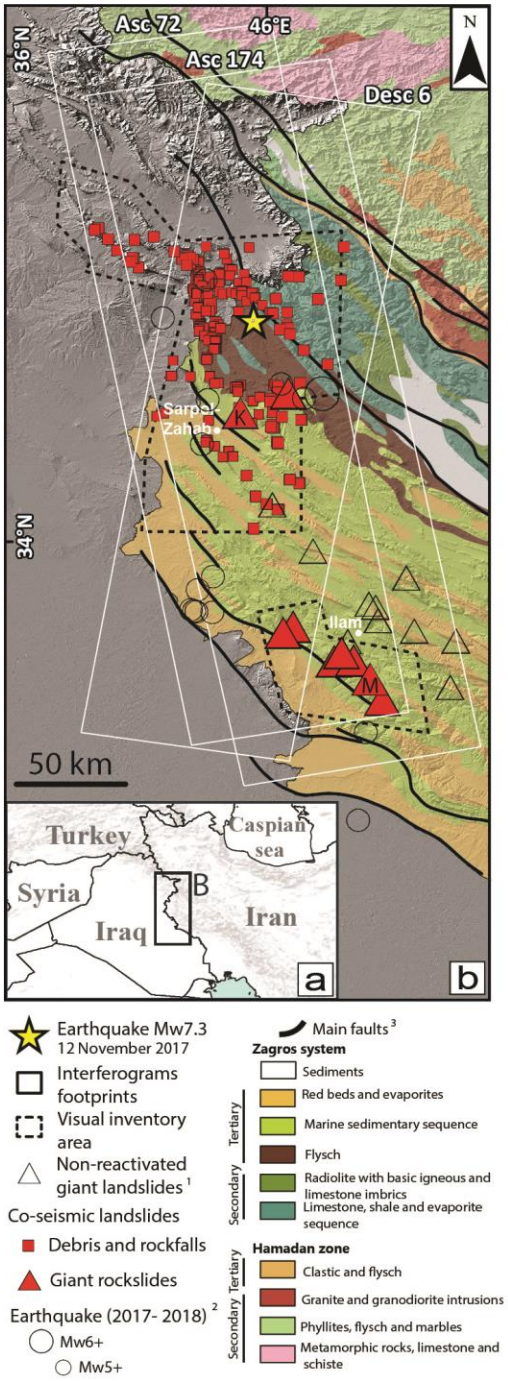

Figure 1. (a) Study area location. (b) Coseismic landslide inventories (geology adapted from the 1:2,500,000 tectonic map of the National Iranian Oil Company, 1978). Empty triangles correspond to giant landslides mapped by Ghazipour and Simpson (2016). The landslides most mentioned in this study are the Mela-Kabod landslide (K) and the Mehr rockslide (M).

Earthquakes (Mw>5; period 2017-2018) are reported from [2]US Geological Survey. The main faults are from [3]Hessami et al. (2003).

2 Geological settings

The Zagros fold and thrust belt (ZFTB, Figure 1) formed in response to the collision between the Arabian and Eurasian plates, which initiated at ~35 Ma (McQuarrie et al., 2003) and continues at the present day with a convergence rate of 8-23 mm/yr (Masson et al., 2014). This N-S convergence produced (1) a succession of asymmetrical, NW-trending, inverted folds affecting a 7-12 km thick pile of sedimentary rocks, comprising limestones, siltstones, shales and salts dating from the Cenozoic to Palaeozoic, and (2) major NW-striking active thrust faults associated with significant seismicity (Mw>6) at the interface between basement and sedimentary cover units at ~20 km depth (Figure 1b; Tavani et al., 2018). The high relief of the Zagros, culminating at about 3650 m altitude, is strongly controlled by resistant calcareous anticlines, which form a succession of ridges separated by narrow valleys developed along the synclinal axes. This semi-arid zone receives about 230 mm/yr of rainfall annually, which falls mostly between November and May. The Mw7.3 Sarpol-Zahab earthquake (12/11/2017) occurred along a near-horizontal blind thrust fault, located between 14-20 km depth (Barnhart et al., 2018; Chen et al., 2018; Gombert et al., 2019; Nissen et al., 2019). Previous studies inferred: (1) a fault rupture of ~50-km-long and ~30-km-wide with a maximum coseismic slip of 5.5 ± 0.5 m, and (2) a high impulsive source with a robust southward rupture directivity which produced the largest ground motions (PGA = ~700 cm/s^2) in the Sarpol-Zahab town (~40 km south from the epicenter). Moreover, high horizontal peak ground accelerations (~100 cm/s^2) were recorded up to 100 km south of the source (Mahani & Kazemian, 2018).

3 Materials and Methods

3.1 Optical Satellite Images Comparison and Correlation

A detailed coseismic landslide inventory was conducted by the visual comparison of PlanetScope satellite images (3 m resolution) acquired before and after the earthquake (19/10/2017 and 13/11/2017) covering an area of 12,000 km^2 centered on the epicenter (see footprint on Figure 1 and Figure S1 in the supporting information). We typically detected and mapped new rockfall scars and debris deposits induced by the earthquake. We also calculated earthquake-induced horizontal ground displacement from the correlation of pre/post-earthquake optical satellite images (Leprince et al., 2007), using both SPOT6/7 images (orthorectified at 1.5 m resolution, following Beyer et al. (2018) see Section S1 for further details), and PlanetScope satellite images-see Table S1, Figure S1, and text S1.

3.2 InSAR Processing

To detect and monitor smaller ground motions associated with earthquake-induced slow-moving landslides, we derived Sentinel-1 InSAR time-series (Doin, et al., 2011) for each landslide using 72 Sentinel-1 SAR images spanning a 20 month time period (beginning 10 months before the earthquake). We generated differential interferograms using the NSBAS (New Small BAseline Subset) (Doin et al., 2011) processing chain based on the ROI_PAC software (Rosen et al., 2004). We used two ascending (174 and 72, subswath iw1 for both) and one descending (6, subswath iw2) tracks of Sentinel 1A and 1B covering an area of 33,500 km2 (see footprint on Figure 1b and Table S1), with a revisit time of 12 days. Initially, we re-sampled all secondary SLC (Single Look Complex) images in a single reference SLC geometry and co-registered secondary to reference using precise orbits and an ASTER digital elevation model (30 m

129 resolution), combined with empirical offsets between secondary and reference images. Then, a
130 small baseline subset is defined using temporal and perpendicular baseline constraints (Doin, et
131 al., 2011). After calculating differential interferograms we corrected them from atmospheric
132 delays using ERA-5 ECMWF reanalysis (Doin et al., 2009). Finally, we made an empirical
133 correction for topographically-correlated atmospheric-delays. The coseismic interferograms were
134 then inspected for landslide-like patterns throughout the region. The coseismic signals were too
135 large to be unwrapped due to phase ambiguities across landslide boundaries. For this reason, we
136 bound the amplitude of the coseismic motion using (1) the number of fringes on the coseismic
137 interferogram (which provides a lower limit), and (2) the optical image correlation (an upper
138 limit). For the same reason, we also analyze the time-series independently to determine the pre-
139 and post- seismic landslide kinematics (see text S5).

140 ### 3.3 Geomorphological Analysis

141 Finally, we conducted geomorphological and geological analysis coupling the stereo-derived
142 high resolution DEMs (text S1), Google Earth satellite imagery and geological maps to better
143 constrain the typology and failure modes of the detected landslides.

144 ## 4 Results

145 ### 4.1 Rockfalls

146 We map 360 coseismic rockfalls, and their associated debris cones (areas ranging between 200-
147 and 20,000 m^2), which affect mainly limestones and flyschs (Figure 1b, S2). About 85% of the
148 detected rockfalls are concentrated within a radius of 40 km (smaller than the fault rupture
149 length) of the epicenter (Figure S3). They mostly occurred on slopes between 40° and 80°,
150 which are significantly steeper than the mean ~18° slope of the area (Figure S4).

151 ## 4.2 Giant rockslides

152 ### 4.2.1 Coseismic Detection

153 Nine instances of coseismic landslide motion were detected (Figure 1b), one from the coseismic
154 correlation of optical images (Mela-Kabod) and eight from the coseismic interferograms analysis
155 (areas between 2-15 km^2, see Table S2). They are all located south of the epicenter, two at ~40
156 km , and the remaining seven clustered between 140-180 km from the epicenter (Figure 1b,
157 Table S2), in a region where no rapid slope-failures were detected in the PlanetScope imagery.
158 The giant Mela-Kabod landslide displays a coseismic motion of about 35 m (Figure S5), a value
159 consistent with previous estimates (Valkaniotis et al., 2018).
160 InSAR analysis reveals activity of 8 landslides, which are generally characterized by 3-4 fringes
161 outlined by sharp phase discontinuities with the surrounding area (Figure 2) during the coseismic
162 period. They correspond to a coseismic motion of at least 30 mm in the Line Of Sight (LOS),
163 reaching more than 100 mm in most cases (Figure 2b, c, Table S2 and text S4). Four of the
164 detected patterns are correlated with giant rockslides from the inventory of Ghazipour and
165 Simpson (2016); the other four reflect newly mapped slope failures (Table S2).

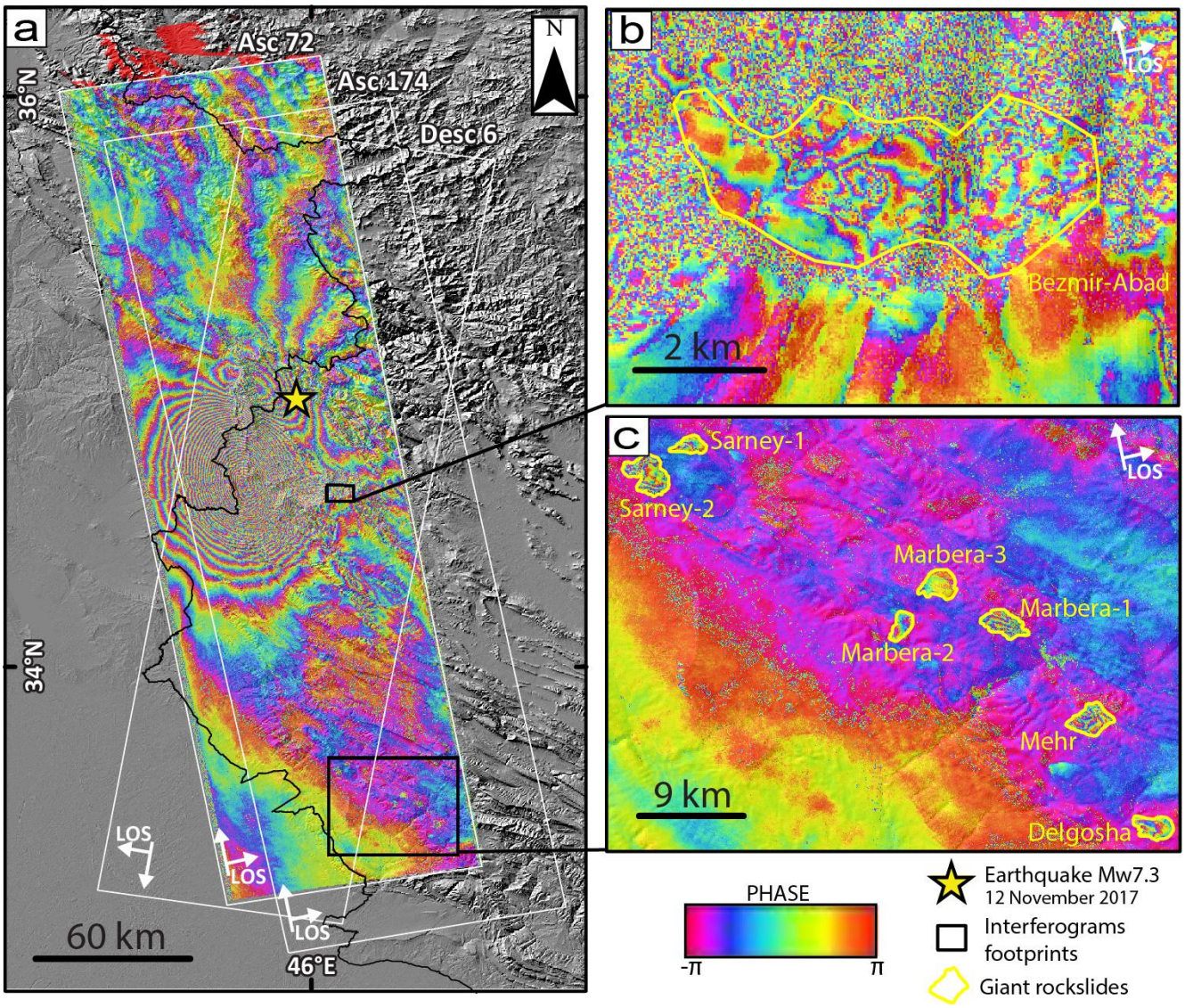

Figure 2. (a) Example of a coseismic interferogram computed over the study area from the ascending track 72 between 11/11/2017 and 17/11/2017 (the looking angle of the radar varies between 27.3°-32.5°). (b) and (c) zooms show the 8 landslides detected with InSAR near the earthquake and in the southern far-field, respectively.

4.2.2 Annual kinematics

The cumulative LOS displacement time-series computed shows different pre- and post-seismic rockslide behaviors. Rockslide velocities range between 0-25 mm/yr, and 2-46 mm/yr for the

pre- and post-seismic periods, respectively (Figure 3 and Table S2). The pre-seismic period shows either dormant rockslides (almost zero velocity within the error limits: Figure 3c, d, e, h) or active rockslides with constant velocities (Figure 3b, f, g, i, j). The coseismic motion is followed by a transient relaxation over 20 days clearly seen at several sites: Mela-Kabod, Marbera-3, Marbera-1 and Mehr (Figure 3c, f, g, i). Following this, three different post-seismic patterns emerge: (1) rockslides with constant post-seismic velocity equivalent to the pre-seismic one (Figure 3b, d, h, i), (2) rockslides with constant post-seismic velocity higher than the pre-seismic one (Figure 3e, j) and (3) rockslides showing a transient increase in velocity of several months before returning to their pre-seismic rates (Figure 3c, f, g). In this latter case, the succession of those two ultimate post-seismic phases coincides with the rainy and dry seasons as shown by the comparison with cumulated rainfall (Figure 3a). Finally, an offset of the last acquisition date at the end of the Bezmir Abad time-series (Figure 3b) may correspond to the co-seismic effects of a Mw6.0 earthquake that occurred 13 kilometers away (Figure 1, S7).

187

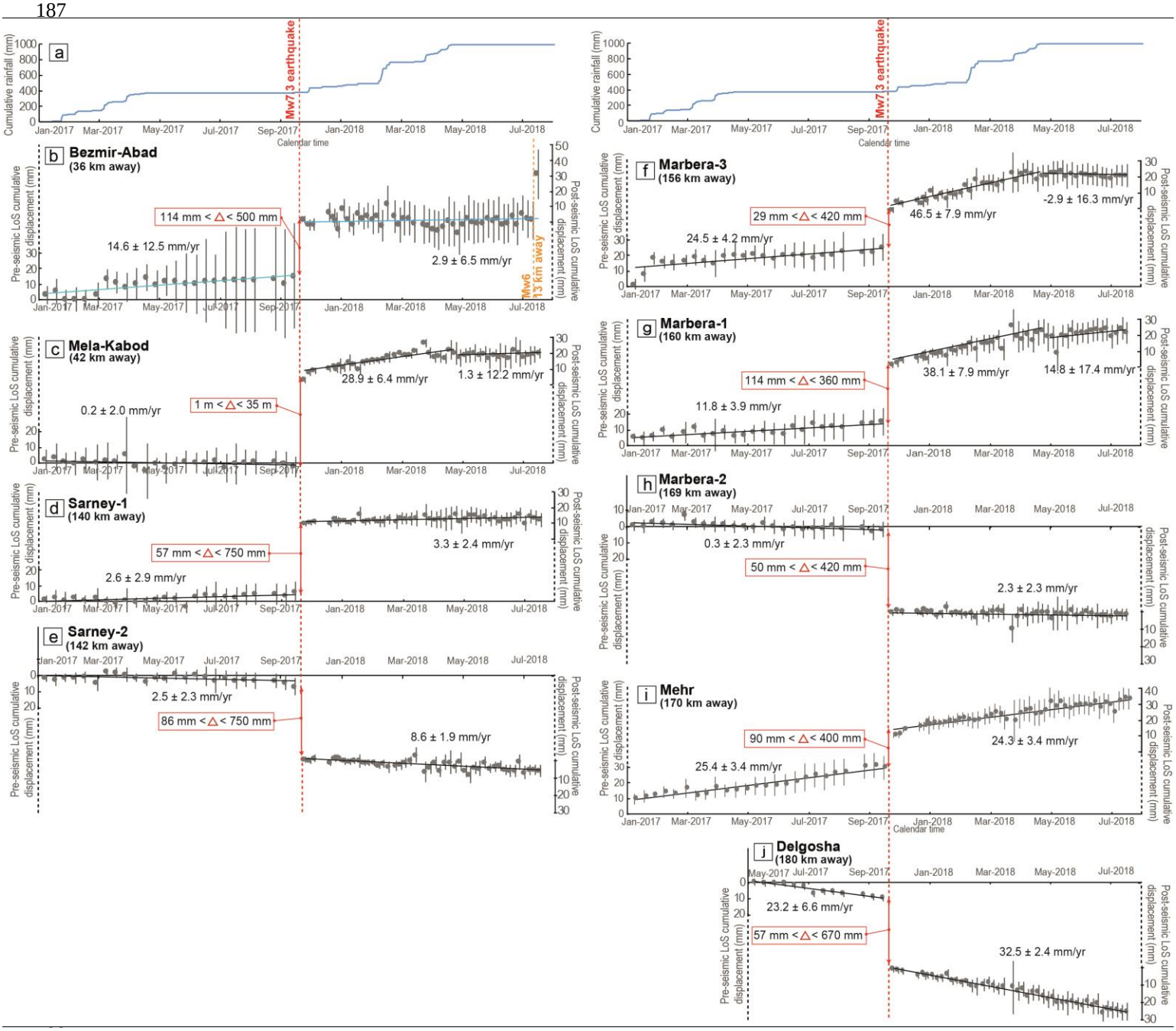

189 Figure 3. (a) Cumulative rainfall collected at the Ilam meteorological station (Figure 1b; National
190 Climatic Data Center). (b) to (j) show the cumulative LOS displacement time-series with the
191 error bars, computed for all the detected rockslides from InSAR over 18 months spanning the
192 Mw7.3 Sarpol-Zahab earthquake and revealing the rockslide coseismic motion (Δ). The pre-

193 seismic InSAR time-series for the Delgosha rockslide (j) span for only 6 months before the
194 earthquake.

195 4.2.2 Geomorphological characterization

196 Results from our geomorphological analysis of the Mehr rockslide, located 170 km south of the
197 epicenter, are shown in Figure 4 (see Figure S6 and table S2 for detailed results of the other
198 rockslides). The coseismic motion extent, clearly visible in the interferogram (Figure 4a),
199 delineates a region 3 km long by 2.5 km wide, which is bounded to the SW by a ~160 m high
200 headscarp and to the northeast by the toe of debris deposits that propagate ~600 m over the
201 valley floor (see DEM in Figure 4b). At the SE limit, the lateral rockslide boundary is well-
202 defined in the geomorphology. The geological map (Figure 4c) and the cross-section (Figure 4d)
203 indicate that the rockslide occured at the contact between Ilam limestones and overlying Surgah
204 shales, along the northern flank of a NW-SE-striking anticline. The rockslide consists of
205 limestone blocks sliding on the shale layer, which dips 5-15° to the NE. Comparison between a
206 topographic profile extracted along the rockslide and another along the undisturbed slope
207 suggests a maximum depth of 200 m for the slip surface (Figure 4d), implying a rockslide
208 volume of ~0.5 km^3.
209 Observations are similar for the other rockslides (Figure S6 and Table S2): (1) all the detected
210 interferometric patterns match the positions of pre-existing giant rockslides with an estimated
211 volume range from 0.16 to 2.2 km^3, and (2) six of those rockslides occur at the contact between
212 limestone and shales from the Ilam and the Surgah formations.

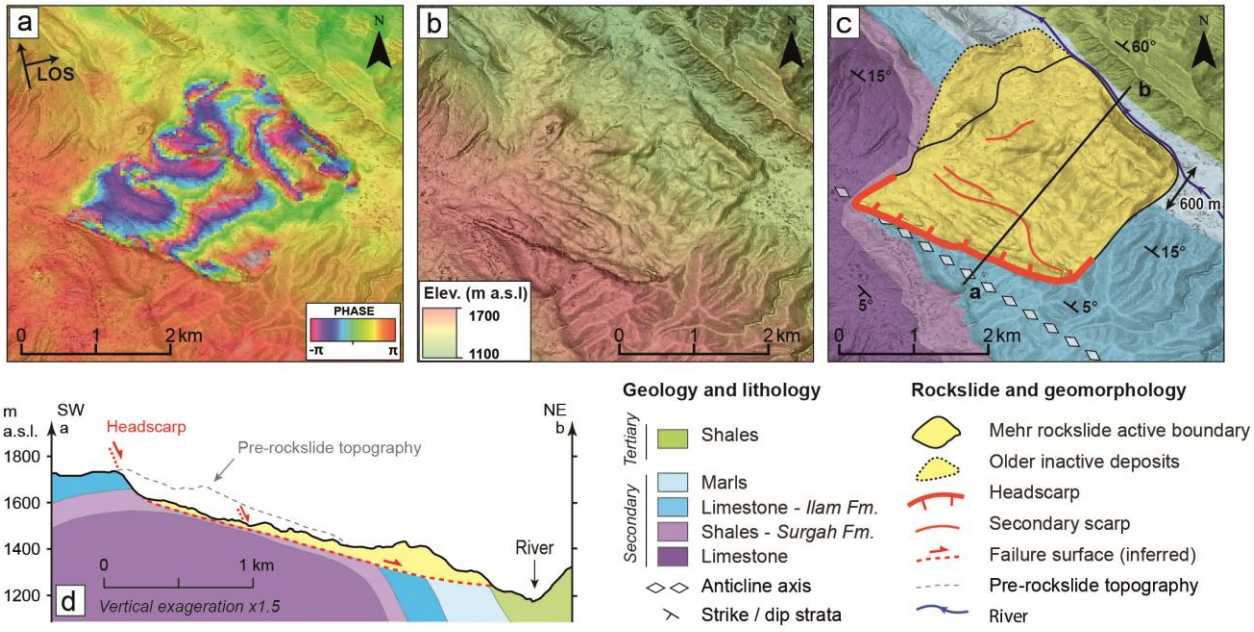

Figure 4. The Mehr giant rockslide (see location in Figure 1b) presented from (a) a coseismic interferogram computed along the Sentinel-1 ascending track-72 between 11/11/2017 and 17/11/2017, (b) a pre-seismic SPOT6-7 hillshaded DEM (4 m resolution, 09/09/2014), (c) a geological map adapted from Llewellyn (1974), (d) a cross-section built along the profile "ab" shown in c.

5 Discussion

5.1 Coseismic landslide database

The Sarpol-Zahab earthquake induced coseismic displacements for two types of landslides: 360 small rockfalls clustered in a radius of a few tens of kilometers around the epicenter, and 9 giant rockslides mainly located in the far-field (up to 4 times the fault length). The high concentration of rockfalls in the epicentral area (compared to the wider zone of fault slip) can be explained by the impulsive source (Gombert et al., 2019), which leads to stronger ground-motions close to the

epicenter. This spatial distribution highlights the dynamic triggering of these rockslides (e.g., Meunier et al., 2007).

The number of recorded landslides is low for a Mw7.3 earthquake, which would be expected to trigger a few thousand landslides in such a mountainous area (Keefer, 2002, Tanyas et al., 2017). This low number may be explained by (1) the aridity of the region, which limits weathering and soil production (Lacroix et al., 2013, Roback et al., 2018), and (2) blind thrust faulting, which induces lower ground motions than surface rupturing earthquakes (Aki, 1987).

5.2 Far-field seismic forcing

The striking feature of this earthquake resides in the coseismic motion of several giant pre-existing rockslides located at epicentral distances of 140 km to 180 km (Figure 1b). Keefer (2002) documents several case studies where small landslides were triggered at large distances from the epicenters, possibly due to low seismic attenuation and/or extraordinary susceptibility of some sites. However, the huge size (~0.1-2 km^3) of the earthquake-induced rockslides here is intriguing and, to our knowledge, has never been reported so far from the epicenter.

Rockslide forcing in the far field south of the epicenter can first be explained by the strong directivity of the rupture toward the south (Chen et al., 2018; Gombert et al., 2019), as well as by the stronger movements perpendicular to the fault (Mahani & Kazemian, 2018), which may favor the triggering of rockslides oriented NE-SW. In the ZFTB geological context, the ground shaking can also be amplified by both local topographic and geological effects (Maufroy et al., 2015; Murphy, 2015), more specifically as the rockslides developed on flanks of anticline ridges and in mechanically heterogeneous lithologies. Calculation of a 1D resonance frequency of the destructured slump body overlying the thick rigid layer shows wave amplifications at low frequencies (text S6), around 1Hz, compatible with the frequency content of the earthquake

source at such large distances (Mahani & Kazemian, 2018), which can thus favor landslide triggering.

Interestingly, several other ancient landslides previously mapped in this region (Ghazipour & Simpson, 2016) were not reactivated during the Sarpol-Zahab earthquake (Figure 1b). However, these landslides mostly occurred in different lithologies (Oligocene and Eocene units) with a structure (thick moderately incompetent layer of calcareous shale underlying the carbonate slump body) less sensitive to sliding and seismic amplification.

Finally, our time-series reveal a transient increase of the post-seismic velocity compared to the pre-seismic annual velocity for at least 5 of the studied rockslides (Figure 3c, e, f, g, j). For 3 of the rocksldies (Mela-Kabd, Marbera-1, Marbera-3) we document a higher velocity during the 2018 rainy season (Figure 3c, f, g) followed by a subsequent decrease in velocity, eventually returning to the pre-earthquake velocity during the dry season. This observation may suggest a seasonal motion and threshold rainfall effects on the landslide kinematics (Zerathe et al., 2016). Furthermore, moderate earthquakes (Mw5-6) that occurred close to the landslides (Figure 1, S7) may have contributed to the transient velocity increase by damaging rock, thus promoting water infiltration (Bontemps et al., 2020) up to the impermeable Surgah formation. However, exploring these issues will require longer time-series as well as detailed field measurements of hydrologic and kinematical parameters (e.g. Schulz et al., 2009).

6 Conclusion

We used a new approach to generate a comprehensive inventory of earthquake-induced landslides, combining InSAR, image correlation and visual change detection. Applying it to the Mw 7.3 Sarpol-Zahab earthquake, we detected 369 coseismic landslides of different sizes and kinematics, including 360 rockfalls and 9 giant rockslides.

The striking element of this earthquake-induced landslide database is the coseismic motion of 9 pre-existing giant rockslides (3-30 km^2) in the far field, all initially generated by sliding of a thick limestone layer over a shale formation on both limbs of anticlinal structures, in directions perpendicular to the anticline axis (i.e. NE-SW). The coseismic motion of these slow-moving giant rockslides (<40 mm/yr) was at least 30 mm, reaching up to 35 m. At least three of them were also accelerated over the rainy season following the earthquake, showing either a seasonal climatic forcing or an increased rainfall infiltration enhanced by the landslide bulk damage produced by the ground shaking. We show that the coseismic motion of these rockslides may be related to a complex combination of the southward directivity of the source, the NE-SW polarization of the motions, their sensitivity to low-frequencies (~1 Hz), and the site effect due to the seismic impedance contrast on the flanks of the anticlines.

The detection of significant coseismic motion of several ancient giant rockslides using InSAR may open new perspectives on the understanding of large-scale gravitational deformations in arid settings. Most of the rockslides investigated here display huge cumulated headscarps (100's m); it is therefore likely that repeated large earthquakes over longer time scales constitute one of the predominant forcings for this displacement. These landslides have certainly been active over several millennia, as observed for other giant landslides of the area (Roberts & Evans, 2013). Dating of landslide headscarps is therefore a key issue in understanding how earthquakes control landslide dynamics on different time scales.

Acknowledgments, Samples, and Data

This research is funded by the Lebanese National Council for Scientific Research (CNRS). The authors also thank the support of the French Spatial Agency (CNES). Supplementary figures, tables and graphs are provided in the supporting information accompanying the main text. The

data archiving is underway on the PerSCiDO platform. Meanwhile, the data are available at the following link https://1drv.ms/u/s!Alv20Xzpi7Jig2gksQk9RHNuN3Ym?e=AanU5p.

References

Aki, K., 1987, Strong Motion Seismology, *in* Erdik, M.Ö., Toksöz, M.N. (eds), *Strong Ground Motion Seismology* (Vol. 204). Dordrecht:Springer. https://doi.org/10.1007/978-94-017-3095-2_1.

Barnhart, W. D., Brengman, C. M., Li, S., & Peterson, K. E. (2018), Ramp-flat basement structures of the Zagros Mountains inferred from coseismic slip and afterslip of the 2017 Mw7. 3 Darbandikhan, Iran/Iraq earthquake. Earth and Planetary Science Letters, 496, 96-107. https://doi.org/10.1016/j.epsl.2018.05.036.

Beyer, R. A., Alexandrov, O., & McMichael, S. (2018), The Ames Stereo Pipeline: NASA's open source software for deriving and processing terrain data. Earth and Space Science, 5(9), 537-548. https://doi.org/10.1029/2018EA000409.

Bontemps, N., Lacroix, P., Larose, E., Jara, J., & Taipe, E. (2020), Rain and small earthquakes maintain a slow-moving landslide in a persistent critical state. Nature communications, 11(1), 1-10. doi:10.1038/s41467-020-14445-3.

Chen, K., Xu, W., Mai, P. M., Gao, H., Zhang, L., & Ding, X. (2018), The 2017 Mw 7.3 Sarpol Zahāb Earthquake, Iran: A compact blind shallow-dipping thrust event in the mountain front fault basement. Tectonophysics, 747, 108-114. https://doi.org/10.1016/j.tecto.2018.09.015.

Doin, M.P., Guillaso, S., Jolivet, R., Lasserre, C., Lodge, F., Ducret, G., & Grandin, R. (2011), Presentation of the small baseline NSBAS processing chain on a case example: the Etna deformation monitoring from 2003 to 2010 using Envisat data. Proceedings of the Fringe symposium, Frascati, Italy: ESA SP-697, 3434-3437.

Doin, M.-P., Lasserre, C., Peltzer, G., Cavalie, 0., & Doubre, C. (2009), Corrections of stratified tropospheric delays in SAR interferometry: Validation with global atmospheric models. *Journal of Applied Geophysics, 69(1*), 35-50. doi:10.1016/j.jappgeo.2009.03.010.

Fan, X., Scaringi, G., Korup, O., West, A. J., Van Westen, C. J., Tanyas, H., et al. (2019), Earthquake-induced chains of geologic hazards: Patterns, mechanisms, and impacts. *Reviews of geophysics, 57(2),* 421-503. https://doi.org/10.1029/2018RG000626.

Ghazipour, N., & Simpson, G. (2016), Size distribution and controls of landslides in the Zagros mountain belt (Iran). *Geological Society of America Special Papers, 525*. doi: 10.1130/2016.2525(13).

Gombert, B., Duputel, Z., Shabani, E., Rivera, L., Jolivet, R., & Hollingsworth, J. (2019), Impulsive Source of the 2017 MW= 7.3 Ezgeleh, Iran, Earthquake. *Geophysical research letters, 46(10),* 5207-5216. https://doi.org/10.1029/2018GL081794.

Goorabi, A. (2020), Detection of landslide induced by large earthquake using InSAR coherence techniques–Northwest Zagros, Iran. *The Egyptian Journal of Remote Sensing and Space Science, 23(2),* 195-205. https://doi.org/10.1016/j.ejrs.2019.04.002.

Gorum, T., Fan, X., Van Westen, C. J., Huang, R. Q., Xu, Q., Tang, C., & Wang, G. (2011), Distribution pattern of earthquake-induced landslides triggered by the 12 May 2008 Wenchuan earthquake. *Geomorphology, 133(3-4),* 152-167. https://doi.org/10.1016/j.geomorph.2010.12.030.

Hessami, K., Jamali, F., & Tabassi, H. (2003), *Map of major active faults of Iran* (scale 1: 2,500,000).

Keefer, D. K. (2002), Investigating landslides caused by earthquakes–a historical review. *Surveys in geophysics, 23(6),* 473-510. https://doi.org/10.1023/A:1021274710840.

Lacroix, P., Perfettini, H., Taipe, E., & Guillier, B. (2014), Coseismic and postseismic motion of a landslide: Observations, modeling, and analogy with tectonic faults. *Geophysical Research Letters, 41(19),* 6676-6680. https://doi.org/10.1002/2014GL061170.

Lacroix, P., Zavala, B., Berthier, E., & Audin, L. (2013), Supervised method of landslide inventory using panchromatic SPOT5 images and application to the earthquake-triggered landslides of Pisco (Peru, 2007, Mw8. 0). *Remote Sensing, 5(6),* 2590-2616. doi:10.3390/rs5062590.

Leprince, S., Ayoub, F., Klinger, Y., & Avouac, J.P. (2007), Co-registration of optically sensed images and correlation (COSI-Corr): An operational methodology for ground deformation measurements. *International Geoscience and Remote Sensing Symposium IEEE, Barcelona*, 1943-1946. doi:10.1109/IGARSS.2007.4423207.

Llewellyn, P.G. (1974). Geological compilation map, Ilam-Kuhdasht (Map NO.20504). Tehran:Oil Service Company of Iran.

Mahani, A. B., & Kazemian, J. (2018), Strong ground motion from the November 12, 2017, M 7.3 Kermanshah earthquake in western Iran. *Journal of Seismology, 22(6),* 1339-1358. https://doi.org/10.1007/s10950-018-9761-x.

Marano, K. D., Wald, D. J., & Allen, T. I. (2010), Global earthquake casualties due to secondary effects: a quantitative analysis for improving rapid loss analyses. *Natural hazards, 52(2),* 319-328. doi:10.1007/s11069-009-9372-5.

Marc, O., Hovius, N., Meunier, P., Uchida, T., & Hayashi, S. (2015), Transient changes of landslide rates after earthquakes. *Geology, 43(10),* 883-886. https://doi.org/10.1130/G36961.1.

Masson, F., Lehujeur, M., Ziegler, Y., & Doubre, C. (2014), Strain rate tensor in Iran from a new GPS velocity field. *Geophysical Journal International, 197(1),* 10-21. https://doi.org/10.1093/gji/ggt509.

Maufroy, E., Chaljub, E., Hollender, F., Kristek, J., Moczo, P., Klin, P., et al. (2015), Earthquake Ground Motion in the Mygdonian Basin, Greece: The E2VP Verification and Validation of 3D Numerical Simulation up to 4 Hz. *Bulletin of the Seismological Society of America, 105(3),* 1398–1418. doi: 10.1785/0120140228.

McQuarrie, N., Stock, J.M., Verdel, C., & Wernicke, B.P. (2003), Cenozoic evolution of Neotethys and implications for the causes of plate motions. *Geophysical research letters, 30(20),* SDE 6.1-SDE 6.4. doi:10.1029/2003GL017992.

Meunier, P., Hovius, N., & Haines, A.J. (2007), Regional patterns of earthquake-triggered landslides and their relation to ground motion. *Geophysical Research Letters, 34(20),* L20408. doi:10.1029/2007GL031337.

Meunier, P., Hovius, N., & Haines, J.A. (2008), Topographic site effects and the location of earthquake induced landslides. *Earth and Planetary Science Letters, 275(3-4),* 221-232. https://doi.org/10.1016/j.epsl.2008.07.020.

Miyajima, M., Fallahi, A., Ikemoto, T., Samaei, M., Karimzadeh, S., Setiawan, H., et al (2018), Site investigation of the Sarpole-Zahab earthquake, Mw 7.3 in SW Iran of November 12, 2017. *JSCE Journal of Disaster, FactSheet: FS2018-E-0002.*

Murphy, B. (2015), Coseismic landslides. *Landslide Hazards, Risks and Disasters* (pp. 91-129). Academic Press. https://doi.org/10.1016/B978-0-12-396452-6.00004-5.

Nissen, E., Ghods, A., Karasözen, E., Elliott, J.R., Barnhart, W.D., Bergman, E.A., et al. (2019), The 12 November 2017 M w 7.3 Ezgeleh-Sarpolzahab (Iran) Earthquake and Active

Tectonics of the Lurestan Arc. *Journal of Geophysical Research: Solid Earth, 124(2),* 2124-2152. https://doi.org/10.1029/2018JB016221.

Roback, K., Clark, M.K., West, A.J., Zekkos, D., Li, G., Gallen, S.F., Chamlagain, D., & Godt, J.W. (2018), The size, distribution, and mobility of landslides caused by the 2015 Mw7.8 Gorkha earthquake, Nepal. *Geomorphology, 301*, 121-138. https://doi.org/10.1016/j.geomorph.2017.01.030.

Roberts, N. J., & Evans, S. G. (2013), The gigantic Seymareh (Saidmarreh) rock avalanche, Zagros Fold–Thrust Belt, Iran. *Journal of the Geological Society, 170(4),* 685-700. doi:10.1144/jgs2012-090.

Rojstaczer, S., & Wolf, S. (1992), Permeability changes associated with large earthquakes. An example from Loma Prieta, California. *Geology, 20(3),* 211-214. https://doi.org/10.1130/0091-7613(1992)020<0211:PCAWLE>2.3.CO;2.

Rosen, P.A., Hensley, S., Peltzer, G., & Simons, M. (2004), Updated repeat orbit interferometry package released. *Eos Transactions American Geophysical Union, 85(5*), 47-47. https://doi.org/10.1029/2004EO050004.

Schulz, W.H., McKenna, J.P., Kibler, J.D., & Biavati, G. (2009), Relations between hydrology and velocity of a continuously moving landslide-evidence of pore-pressure feedback regulating landslide motion?. *Landslides, 6*, 181–190. https://doi.org/10.1007/s10346-009-0157-4.

Tanyas, H., Van Westen, C.J., Allstadt, K.E., Anna Nowicki Jessee, M., Görüm, T., Jibson, R.W., et al. (2017), Presentation and analysis of a worldwide database of earthquake-induced landslide inventories. *Journal of Geophysical Research: Earth Surface, 122(10),* 1991-2015. https://doi.org/10.1002/2017JF004236.

Tavani, S., Mariano Parente, M., Puzone, F., Corradetti, A., Gharabeigli, G., Valinejad M., et al. (2018), The seismogenic fault system of the 2017 Mw 7.3 Iran–Iraq earthquake: constraints from surface and subsurface data, cross-section balancing, and restoration. *Solid Earth, 9,* 821–831. https://doi.org/10.5194/se-9-821-2018.

Vajedian, S., Motagh, M., Mousavi, Z., Motaghi, K., Fielding, E., Akbari, B., et al. (2018), Coseismic deformation field of the Mw 7.3 12 November 2017 Sarpol-e Zahab (Iran) earthquake: A decoupling horizon in the northern Zagros Mountains inferred from InSAR observations. *Remote Sensing, 10(10),* 1589. doi:10.3390/rs10101589.

Valkaniotis, S., Ganas, A., Tsironi, V., & Barberopoulou, A. (2018), A preliminary report on the M7.5 Palu 2018 earthquake co-seismic ruptures and landslides using image correlation techniques on optical satellite data. *EMSC*. https://doi.org/10.5281/zenodo.1467128.

Wang, C. Y., & Chia, Y. (2008), Mechanism of water level changes during earthquakes: Near field versus intermediate field. *Geophysical Research Letters, 35,* L12402. doi:10.1029/2008GL034227.

Wang, G., Zhang, D., Furuya, G., & Yang, J. (2014), Pore-pressure generation and fluidization in a loess landslide triggered by the 1920 Haiyuan earthquake, China: a case study. *Engineering Geology, 174,* 36-45. https://doi.org/10.1016/j.enggeo.2014.03.006.

Zerathe, S., Lacroix, P., Jongmans, D., Marino, J., Taipe, E., Wathelet, M., et al. (2016), Morphology, structure and kinematics of a rainfall controlled slow-moving Andean landslide, Peru. *Earth Surface Prosses and Landforms, 41(11),* 1477-1493. https://doi.org/10.1002/esp.3913.

Supporting Information References

Geli, L, Bard, P.Y., & Jullien, B. (1988), The effect of topography on earthquake ground motion: A review and new results. *Bulletin of the Seismological Society of America, 78 (1)*, 42–63.

Kramer, S. L. (1996). Geotechnical earthquake engineering. In *Prentice–Hall international series in civil engineering and engineering mechanics* (Chapter 6, pp. 226– 228). New Jersey: Prentice-Hall.

Socco, L. V., Jongmans, D., Boiero, D., Stocco, S., Maraschini, M., Tokeshi, K., & Hantz, D. (2010), Geophysical investigation of the Sandalp rock avalanche deposits. *Journal of Applied Geophysics, 70(4)*, 277-291. https://doi.org/10.1016/j.jappgeo.2009.12.005.

Telford, W.M., Geldart, L.P., Sheriff, R.E., & Sheriff, R.E. (1990), *Applied geophysics.* London:Cambridge university press. doi:10.1017/CBO9781139167932.